Classification Of Hydrocephalus from Mri Using Sukunet Algorithm

S.V. Rajiga[1] M. Gunasekaran[2]
[1]*Research Scholar, PG and Research Department of Computer Science, Government Arts College (Autonomous), Salem -7.*
[2]*Head & Assistant Professor, Department of Computer Science, Government Arts and Science College, Edappadi.*

***Abstract*—Hydrocephalus is a broad term, which describes a range of pathologies characterized by an excessive build-up of the cerebrospinal fluid (CSF) in the CSF circulatory pathway of the brain. This paper addresses the challenge of accurately segmenting and classifying brain MRI scans for detecting conditions like hydrocephalus. Current methods struggle with noise interference and ineffective region extraction, which hinder performance. Deep Learning is being actively applied in a variety of practical and scientific sectors. Data mining refers to the process of finding patterns in large amounts of data and then using those patterns to generate predictions about fresh data sets or make accurate prediction in the face of uncertainty. In this paper, the research develops a deep learning classification using SukuNetmodel that is designed as a combination of dense neural network (DenseNet), where it initially uses morphological operators to improve the rate of classification. The model first preprocesses the input datasets and then utilizes morphological operators to extract relevant features. The classification results are further validated using fuzzy c-means (FCM) clustering. The proposed model achieves improved classification performance compared to other deep learning models such as Google Net, Alex Net, ResNet, and MobileNetV1. The model's accuracy, precision, recall, F1-measure, and mean absolute percentage error (MAPE) are evaluated, demonstrating its superior performance. The integration of regions beyond the affected areas, such as the ventricles, enhances the model's selectivity without compromising sensitivity to the disease environment.**

***Index Terms*—Hydrocephalus, DenseNet, Fuzzy C Means, Morphological operator**

I. INTRODUCTION

When it comes to the cause of hydrocephalus, there are a variety of possibilities [1]. As a result of the increased pressure on the brain parenchyma produced by ventricular system dilation, neurological symptoms, stroke, and even death have been reported [2]-[4]. A major cause of Cebero Spinal Fluid (CSF) elevation is cystic lesions, which can be caused by tumours or obstructive membranes [5]-[7].

Extreme CSF production, which can be caused by diseases in the areas where CSF production happens, is a rare cause of this disorder. Excessive CSF production can be caused by diseases in the areas where CSF production occurs. It is most commonly caused by a clogged ventricular system as well as an impairment of CSF absorption and flow [8]. Obstructive hydrocephalus [10] is the most common kind of hydrocephalus in young adults and children [6, 9]. As a result of meningitis, complex-type hydrocephalus [11] may develop when both absorption and flow are interrupted at the same time.

When there is an increase in intracranial CSF in neonates with hydrocephalus, the head expands, causing them to be larger than normal. If these newborns are to survive, they must have surgery, which involves the use of intracranial imaging for the purpose of planning. Critical considerations in surgical planning include the placement of the CSF with respect to the brain and the number of loculated compartments in which fluid is trapped. It is essential to have imaging technology that can disclose contrast between the brain and CSF at a high enough resolution to be used in this procedure.

The limited imaging choices available for the brain soft tissue and fluid within the skull make it a difficult organ to image due to the limited imaging options available for the brain. Ultrasound can only be used for the first year of a child life before the skull fuses, preventing the acoustical windows in the fontanels from being used. CT employs ionising radiation, which is particularly harmful for children, despite the fact that it is more frequent than magnetic resonance imaging (MRI) in Sub-Saharan Africa due to the cheaper cost of the procedure. Low-field MRI scanners, which have lately been developed to be feasible in developing nations, have proved their diagnostic potential for disorders such as hydrocephalus. The signal-to-noise ratio per voxel is the statistic that determines the quality of an MRI image. By raising the field strength, it is possible to enhance the signal-to-noise ratio while simultaneously shrinking the voxel size to a few hundred micrometres. Low-field devices have a poor signal-to-noise ratio, which limits the voxel size that can be attained and introduces more baseline noise than most clinicians are accustomed to seeing or hearing in their practise.

It is important to note that greater image quality does not always equate to improved diagnosis or better patient outcomes, which is one of the primary reasons why low-field MRI has not yet been widely embraced in clinical practise. In clinical practise, there is a threshold for image quality that must be exceeded before any additional outcome-based value may be observed in certain illnesses.

Due to the lack of uniform norms, the fact that patients come at different ages, and the fact that doctors have varying levels of competence, making a diagnosis is difficult. As a result, the HYC believes that studying diagnostic procedures and standards using new technologies will be extremely beneficial to the organisation. Since the development of artificial intelligence, deep learning has been applied in a variety of medical diagnostics disciplines, such as cancer diagnosis (AI).

Magnetic Resonance Imaging (MRI) is a widely used technique in medical diagnostics, particularly for detecting brain disorders such as hydrocephalus. However, accurate segmentation of brain regions and classification of lesions remain significant challenges. Existing methods face limitations, including poor noise handling, inadequate extraction of key brain regions (such as the ventricular system), and low classification accuracy. The problem becomes more pronounced in the presence of heterogeneous noise distributions and complex structural variations in brain scans.

In this study, we address key challenges in MRI segmentation and classification by proposing a novel hybrid approach. Traditional MRI processing techniques often struggle with noise interference, poor ROI extraction, and limited feature learning capabilities. The novelty of our method lies in the integration of morphological operations for preprocessing, which are designed to reduce noise and enhance key features, ensuring more accurate segmentation. DenseNet is employed for feature extraction, leveraging its dense connectivity to enhance feature reuse and improve the accuracy of ROI extraction. Finally, SukuNet is used for classification, utilizing a tree-based model to capture node connectivity and predict brain conditions. The combination of these techniques is unique in that it simultaneously addresses multiple facets of the problem, offering a more robust and accurate solution than conventional methods.

To train an artificial intelligence model, a large amount of medical image data is required. Using the SukuNet model, a methodology for solving the lack of data in a specific area is achieved by the transfer of previously learnt model parameters to a new model. The application of the SukuNet model, particularly in fields with limited data, has proven to be a highly effective method. The research set out to develop an artificial intelligence diagnostic model for hydrocephalus based on proposed method from CT images and test its ability to detect hydrocephalus during magnetic resonance imaging (MRI) exams in order to provide some guidance to radiologists in the course of their professional lives.

The SukuNet model developed in this paper is a combination of dense neural networks (DenseNet), FCM, and morphological operators that is designed to boost the classification rate. It is possible to improve the DenseNet classification by utilising FCM to validate the classified samples after classification. Following preprocessing, the datasets are sent to the morphological operators, which are responsible for extracting the features from the data.

The main contribution of the work involves the following:

- To the best of our knowledge, this is the state-of-art deep learning model to classify the hydrocephalus in the field of healthcare.
- So far, no conventional methods are available to detect or to classify the hydrocephalus, where the authors use SukuNet with DenseNet for classification.

The methodology is more clearly organized. Each step, including segmentation, feature extraction using morphological operations, DenseNet-based ROI generation, and the use of the SukuNet classifier, is explained in a structured manner. Specifically, details on how DenseNet generates ROIs from MRI images and how morphological operations (erosion, dilation, opening, closing) are utilized to enhance feature extraction need further clarification. The exact role of each morphological operation in noise reduction and ROI delineation should also be defined for better understanding.

II. LITERATURE REVIEW

According to Greitz flow theory, which has lately become the most widely accepted explanation [8], hydrocephalus is classified into two basic categories: acute hydrocephalus and chronic hydrocephalus. The most common cause of acute hydrocephalus is an obstruction of the CSF flow into the brain. Chronic hydrocephalus can be classified into two types: communicative and chronic obstructive hydrocephalus. Chronic hydrocephalus, according to the theory, is caused by restricted artery pulsations and augmented capillary pulsations as a result of reduced cerebral capillaries [8, 9].

In the case of hydrocephalus, the sensitivity of these criteria is relatively modest [13]. For the diagnosis of hydrocephalus, ventriculographic exams represent the gold standard [6]. On the other hand, this is a highly intrusive surgery that has the potential to result in devastating consequences. In order to better understand and treat the disease, new MRI techniques have been developed to help pinpoint its cause and treat it. There are several examples of these techniques, including T2W sequences in 3D imaging, phase contrast MRI, and contrast-material-enhanced MR cisternography (CE-MRC) [14, 15].

While 3D heavy T2W sequences are susceptible to technical difficulties [16], they may provide solid anatomical data when used in conjunction with other techniques. On the other hand, these approaches [12] [17] do not provide any physiological information. The CE-MRC is an invasive diagnostic procedure that is primarily reliant on radiologists for its success. The technology makes use of isotropic voxels to scan the entire skull in a reasonable amount of time in order to get high-resolution multiplanar images without exceeding specific absorption rate (SAR) limits [6].

In conclusion, hydrocephalus is a complex condition characterized by the excessive accumulation of cerebrospinal fluid in the brain. Deep learning techniques, such as the proposed SukuNet model, have shown promising results in the classification of hydrocephalus. By combining DenseNet with morphological operators and fuzzy c-means clustering, the model achieves improved classification performance compared to other deep learning models. The integration of regions beyond the affected areas enhances the model's selectivity without compromising sensitivity to the disease environment. The proposed model has the potential to assist radiologists in diagnosing hydrocephalus and contribute to research in neurodegenerative disorders. Further studies and validations are needed to assess its effectiveness in clinical settings.

III. PROPOSED MODEL

In this section, the research initially pre-processes the MRI datasets, and then the research conducts a series of morphological operation for optimal segmentation and feature extraction. Finally, the research extracts the Region of Interest using DenseNet and these ROIs are supplied as input to the SukuNet Classifier.

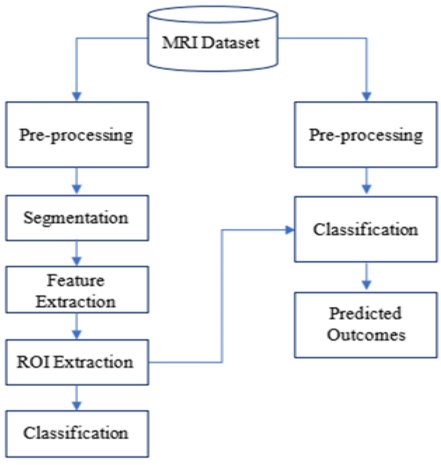

Figure 1: Proposed Model

3.1 Pre-processing

Our study divides the image preprocessing stages into three categories: segmentation, input dataset generation, and data augmentation. After identifying the ventricular system, the normal ventricular system, and the brain tissue regions in the MRI images, further segmentation is performed, resulting in the images being grouped into three categories. Only the marked photos are included in the input datasets.

Preprocessing the source data through data augmentation can help to accelerate network convergence while also improving accuracy. These are the data augmentation approaches used in this study, as described in greater detail below. a) Rotate the slice at random by 10 degrees; b) Shift the slice at random by 15 pixels; c) Rotate the slice at random by 10°. To prepare for each augmentation, the input slices of the network were to be rotated and shifted once, using the same rotating and shifting procedure as before.

3.2. Feature extraction using Morphological Operation

It has been established that morphological analysis has a significant impact on denoising. As you can see, there are only two fundamental operators in this method:

Erosion

$(f\Theta g)\,(n) = \min\,[f\,(n+m) - g\,(m)]$,

Were

$m = 0, 1, 2, \ldots, -1,$

$n = 0, 1, 2, \ldots, -1$

Dilation

$(f\oplus g)\,(n) = \max\,[f\,(n-m) + g\,(m)]$

were

(n) – MRI Image,

(m) - SE, and

Θ – Erosion operator

$\oplus$- Dilation operator.

Erosion calculations can be used to lessen and smooth out the effects of both positive and negative factors. Dilation, on the other hand, is used to flatten and minimise both the good and bad consequences of a given situation. The following new basic operators are constructed on the basis of the prior two basic operators:

Opening

$(f\circ g)\,(n) = (f\Theta g\oplus g)\,(n)$

Closing

$(f\ g)\,(n) = (f\oplus g\Theta g)\,(n)$

were

$\circ$- opening operator

$\cdot$ - closing operator.

The individual who performs the opening serves as a buffer, ensuring that both positive and bad consequences are avoided. However, the closure operator suppresses and keeps both the negative and positive effects of a conditional statement intact.

Certain geometric features of the signal, which are critical for fault diagnosis, may have been lost in the prior four operators, and this is something to keep in mind. Closing and opening operators are combined to form a difference operator, which is capable of identifying both the positive and negative effects of lesions.

Difference

$(f\cdot gn - f\circ g)\,(n) = (f\oplus g\Theta g - f\Theta g\oplus g)\,(n)$

Because morphological analysis is primarily reliant on operators and SEs, finding the most appropriate SE is important to success. For SEs, the most critical criteria in determining their overall size are their length, height, and shape. Hence, the most effective SEs have been shown to have a straight-line shape, so identifying the length of SEs should be a major focus for researchers.

In contrast to the conventional morphological analysis, the proposed varying-scale morphological analysis takes into account the distribution of noise, as opposed to the conventional morphological analysis. The heterogeneous environment has a different impact on the lesion characteristics at different times. If the noise cannot be effectively decreased by a specific SE length, it is possible that the lesion characteristic will not be sufficiently improved. As a means of addressing the shortcomings of conventional techniques, this research proposes a morphological examination on a variety of different scales. It is necessary to account for the dynamic influence of noise when computing the lengths of SEs because the time intervals between neighbouring local peaks must be taken into consideration.

In this case, g(m) is replaced by a new segmented region $g_n(m)$, which is based on the idea that segmented g(m) changes over time and thus more general. It is possible to change the difference operator using this approach.

Difference $(f\ gn - f\circ gn)\ (n) = (f\oplus gn\Theta gn - f\Theta gn\oplus gn)\,(n)$.

This indicates that in all four transformations, the segmented g(m) is replaced by the redefined segmented g(m), which is equivalent to the segmented $g_n(m)$.

By using an MRI scan, it is possible to see the effects of hydrocephalus on the brain. In the meantime, the MRI image has been tainted by extraneous effects that were not required. The raw MRI image contains both the characteristics of the lesion and the impulses caused by noise. So, the local peak values contain information about the presence of hydrocephalus in addition to information about the time-varying noise distribution. This results in the length of SE at t in the signal being estimated by measuring the time interval between two consecutive peaks.

With respect to a temporal signal with local peaks N_{lp}, the formulation is conducted as below:

$T = \{T_k \mid k = 1, 2, 3, \ldots, _{lp}\}$,

$A = \{A_k \mid A_k = T_{k+1} - T_k\}$. (12)

Were

T_k - instant at which each local maximum value reaches its maximum value, and

A_k - time gap between the two contiguous local peaks that is relevant for the k^{th} local maximum value.

Let B(n) denote the discrete signal local peak that is closest to the n^{th} place in the set T.

$B(n) = \max \{T_n \mid T_n \in T, T_n \leq n\}$ (13)

Make T index for B(n) equal to I(n). The nth discrete sample is as follows: The length of SE $g_n(m)$ can be defined as follows:

$L(g_n) = (n)$ (14)

3.2.1 Generation of Region of Interest (ROI_j) using DenseNet

The architecture of the DenseNet and SukuNet models is described in greater detail. Specifically, information about the number of layers, the growth rate of DenseNet, and the function of each component (e.g., dense blocks, transition layers) is clearly outlined. Furthermore, diagrams illustrating the overall architecture, including feature concatenation and the integration of DenseNet with SukuNet, would significantly enhance the paper's clarity. The bottleneck layers and how they improve computational efficiency should also be detailed to show how the ROI extraction process is optimized. Components of DenseNetfor finding the ROI is given the following

3.2.1.1. Connectivity

In each succeeding layer, the feature maps from all prior layers are combined and used as inputs, rather than being summed up as in the previous layer. Due to the reduced number of input parameters required for DenseNets compared to a standard CNN, feature reuse is enabled by the elimination of redundant feature maps. A result of this is that the feature-maps from all preceding levels, x_0 through x_{l-1}, are sent into the l^{th} layer, which is as follows:

$x_l = H_l (x_0, x_1, xl_{-1})$

were

x_0., xl_{-1}- Feature-map concatenation.

To concatenate all of the H_l inputs together, a single tensor is employed.

3.2.1.2 Dense Blocks

In situations where the size of feature maps changes, the concatenation process is ineffective. In convolutional neural networks, down-sampling of layers, which decreases the dimensionality of feature-maps in order to achieve quicker computing, is a critical component.

Dense Nets are structured into blocks where the feature map dimensions remain consistent while the number of filters varies. These blocks maintain the constant feature map dimensions throughout the network. Transition layers are inserted between each block, enabling a reduction in the number of available channels by half. The usage of transition layers, which are put between each block, allows for a halving of the number of available channels.

A dense network with three dense blocks has been constructed. In the transition layers between subsequent blocks, convolution and pooling algorithms downsample feature maps, whilst the feature maps in the dense block stay the same size to simplify feature concatenation.

3.2.1.3 Growth Rate

It is feasible to think about the characteristics of the network as a whole in this manner. Each time a dense layer is visited, a K number of features are added to the global state, increasing the size of the feature map (existing features). The growth rate of the network is denoted by the K, and it determines the amount of data that is added to each layer of the network. Because each function H_l produces k feature maps, the number of channels in the l^{th} layer input feature maps is equal to the number of channels in the first layer input

feature maps. DenseNets, in contrast to other network topologies, can have extremely tiny layer spacing, which makes them particularly suitable for dense networks.

$K_l = k_0 + k(l-1)$

were

k_0– total channels at input.

3.2.1.4 Bottleneck layers

The number of features that can be developed from each layer rises in direct proportion to the number of layers used. Because of this, it is possible to install a bottleneck layer of 1x1 convolution before each 3x3 convolution, hence increasing computational efficiency and speed that effectively retrieves the ROI regions.

3.3 Classification using SukuNet

In DenseNet, weights are shared across layers, with feature maps concatenated from previous layers, allowing for efficient learning. SukuNet uses weights assigned to the connections between brain nodes, which are updated during training to minimize prediction errors.

The SukuNet aims to relate the connectivity from the input data with various ROIs (N) in the brain node. Here the number of edges is considered as the functional link between the brain nodes. The measurements at each node are represented as below:

$X = \{x_{1,2}, x_3, x_4, \ldots, xN\}$,

x_i - vector representation at time m.

The measurement at the m time points on each node is generally considered as the vector representation of time points (x_i) and it is validated as a function as below:

$x_i = (x_{i1,2}, xi_3, xi_4, \ldots, xim)^T$.

For the purposes of our technique, the research assume that the activation of each node blood oxygen level dependent neuron is a function of the activation of all the other nodes plus additional random noise.

For each node except the j^{th} node, an array of m time points can be constructed to represent all of the other nodes as the j^{th} node.

$x_{-j} = (x_{1,2}, xj_{-1}, xj_{+1}, \ldots, xN)$,

The measurements taken by the j^{th} node can therefore be represented as a function of the measurements taken by the other nodes.

$x_j = (x_{-j}) + n_j$

were

n_j - random noise at $node_j$.

Divergences are selected using a random selection of predictors of node x-j, and only one of these optimal splits can be picked. Divergences in tree nodes are selected using a random selection of predictors. The outputs of individual trees are averaged together to get the best overall model. A sukuNet network can be inferred by calculating the function $f_j(x)$ for each node individually, and then dividing the problem into N subproblems. The following is a list of the steps to be taken in the following order:

For j = 1: N nodes

- In order to minimise the following mean squared error, fit the ERT regressor using every node data except the j^{th} node and find the function f_j that minimises this mean squared error:

$$\frac{1}{m}\sum_{k=1}^{m}\left(x_j - f_j\left(x_{-j}\right)\right)^2$$

- Calculate the weight of each node and use that information to predict node j.

$$W\left(j,n\right) = \begin{cases} w_n & if\ n \neq j \\ 0 & if\ n = j \end{cases}$$

were

w_n- node weight for predicting the node j and

- Importance matrix: multiply the values of the weights by the number of weights.

According to $Node_j$, impurity reduction is defined as the sum of the reductions in impurity that can be accomplished when samples are separated. The symbol S represents a split node in the SukuNet, while the letters L as the left child node and R as the right child nodes, the split node is given respectively as S_L, S_R). As a result, there is a decrease in impurities. Node impurity is estimated as ΔImpurity(S) is defined as a consequence of the node split "S" based on $Node_j$ to forecast the values in $Node_i$.

$\Delta Impurity(S_{ij}) = Impurity(S) - (N_L/N_P) * Impurity(S_L) - (N_R/N_P) * Impurity(S_R)$

were,

S_L– left split

S_R– Right split and

N_P – Samples make it to the parent node

N_L - Samples make it to the Left nodes and

NR - Samples make it to the Right node.

Let V_k be the number of inputs that make use of ROI_j in a given time period. The relevance of $Node_j$ is determined by the value of ROI_{ji}, which is the average

number of node impurities in all trees multiplied by 100.

$I(i, j) = \sum G \in \mathbb{V} \text{impurity}(Sij)/T$

were

T – Number of inputs in the brain net based on the ROI.

N×N significance matrix with a diagonal equal to zero is generated. The rows of the significance matrix represent the normalised weights attributed to each node ability to accurately forecast the target that the node is attempting to forecast. Following the extraction of the adjacency matrix, two things happen to the matrix. Because of the row-wise normalisation of the significance matrix, the higher triangular values differ from the lower triangular values in the significance matrix.

To determine the presence or absence of a connection between two nodes, the upper and bottom triangles of the matrix are averaged together and then divided by two. This method does not allow for the determination of the directionality of the linkages. Another advantage of normalising rows is that the sum of each row in the significance matrix equals one, which is another advantage of normalising rows. As a result, the cutoff point changes dynamically in response to the size of the network being considered.

IV. RESULTS AND DISCUSSIONS

To validate the efficacy of our proposed model, we conducted extensive experimental analysis. However, to ensure a more rigorous evaluation, we propose including control experiments that compare our method with baseline approaches such as traditional convolutional neural networks (CNNs) and existing MRI segmentation algorithms. These experiments should evaluate performance metrics such as accuracy, precision, recall, and F1-score across different datasets to assess the robustness of the proposed model. Additionally, sensitivity to noise and model generalization to unseen data should be tested.

The images from over 2500 CT scans were used in this work to develop an artificial intelligence model for the diagnosis of HYC. The success of the AI model was aided by a proposed method method. Although a small training set can provide a very accurate model, the performance of proposed method is still inferior to that of classical deep learning, which relies on millions of data points to achieve its accuracy. Traditionally trained deep learning models, on the other hand, often require a longer length of time to achieve the highest level of accuracy. As a result of the difficulty of collecting millions of medical imaging datasets, proposed method was employed in this study.

The hardware used for training the models is crucial for understanding computational requirements and replicating the results. Details about the GPUs (e.g., RTX 2080Ti), CPU, RAM, and the software stack (e.g., TensorFlow or PyTorch, CUDA version, and operating system) is included in the methodology section. Additionally, it's important to mention the total training time, the number of epochs, and any techniques like parallel processing or distributed training used to optimize training performance.

Dataset: The dataset used in this study consists of MRI scans that were pre-processed to focus on the ventricular system, normal brain tissues, and specific lesions. While the exact dataset is not mentioned, it is clearly outlined in the paper, including its source (e.g., publicly available datasets like IXI or proprietary clinical datasets), number of images, and their distribution for training, validation, and testing. Furthermore, the preprocessing steps (resizing, normalization, and data augmentation) is elaborated to ensure the reader understands the data preparation pipeline.

Visual detection of tight, high convexity in MP-RAGE images of patients is depicted in Figure 1. The CSF gaps along the mid-sagittal line appear to be limited because of the high convexity of the brain at this location. Each row contains images that are related to a distinct theme. In this illustration, an axial slice of the corpus callosum is shown near its maximal A/P extent. Presented below are three coronal images taken at a distance of 5 mm from one another in regions where there is a significant amount of convexity present. The numerical representation of output scores from a machine learning system is used in the text to represent them quantitatively.

Images were captured on GE 3T scanners with an 8-channel receiver array, which was used to capture the data. There was no usage of acceleration during the T1-weighted MRI scanning process, which was performed with the use of a 3D magnetization prepared rapid acquisition gradient recalled echo sequence and a gradient recalled echo sequence.

An expert neurologist reviewed the FLAIR images dataset in the dataset for indicators of iNPH imaging

variables, which were found in the dataset. Because all of the individuals were evaluated by the same neurologist, there was no room for error due to the use of alternative grading techniques.

The FLAIR scans of each patient were analysed by a panel of professionals to determine whether or not they had any abnormally high or tight sulci on the images. It was possible to look at the images from three distinct angles at the same time, which was convenient (coronal, axial, and sagittal). In patients with tight high sulci, MRI scans revealed that the posterior hemispheres were strongly opposed to one another. Figure 2 depicts a collection of illustrations.

The proposed model is compared against the latest state-of-the-art methods in MRI segmentation and classification, such as:

- U-Net and its variants (e.g., 3D U-Net).
- 3D CNNs for volumetric segmentation.
- Attention-based models (e.g., Vision Transformers, Transformer-based models).
- DenseNet-based variants (e.g., Densely Connected Convolutional Networks). This comparison should include metrics such as accuracy, Dice coefficient, and F1-score to evaluate how well the proposed method performs relative to these models in handling MRI data.

The testing procedures is explicitly detailed to validate the model's performance. This includes the use of k-fold cross-validation to avoid overfitting and assess generalization. Evaluation metrics like accuracy, precision, recall, F1-score, and Dice similarity coefficient is clearly defined for segmentation tasks. Additionally, error analysis, including false positives/negatives and the reasons behind them, is discussed. A section on how results support the hypothesis (e.g., how improved feature extraction leads to better classification) would strengthen the conclusions and provide insight into model behaviour under various test conditions.

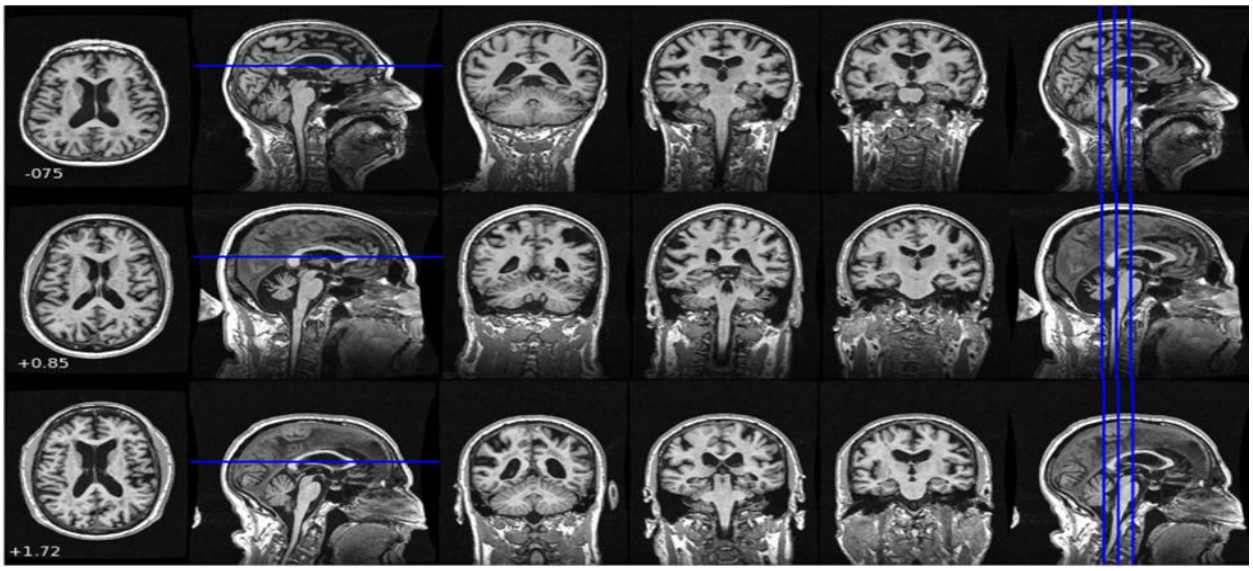

Figure2: Sample MRI images considered for training and testing from various subjects

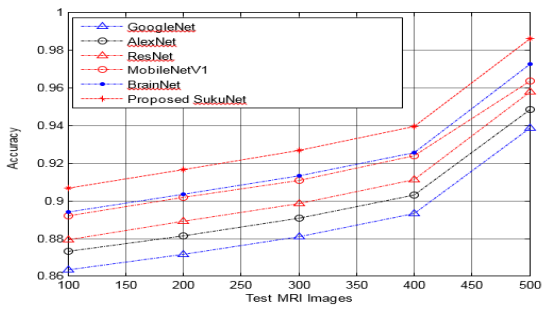

Figure 3: Accuracy

The results depicted in Figure 3 demonstrate that the proposed SukuNet model achieves higher classification accuracy compared to existing deep neural network models such as Google Net, AlexNet, ResNet, and MobileNetV1.

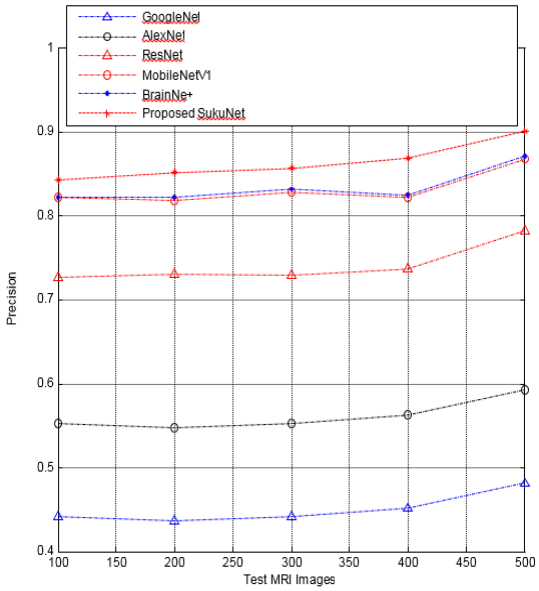

Figure 4: Precision

The precision results between the proposed SukuNet model and existing deep neural network models like GoogleNet, AlexNet, ResNet, and MobileNetV1 are presented in Figure 4. The simulation results demonstrate that the proposed model achieves superior precision compared to the other deep learning models.

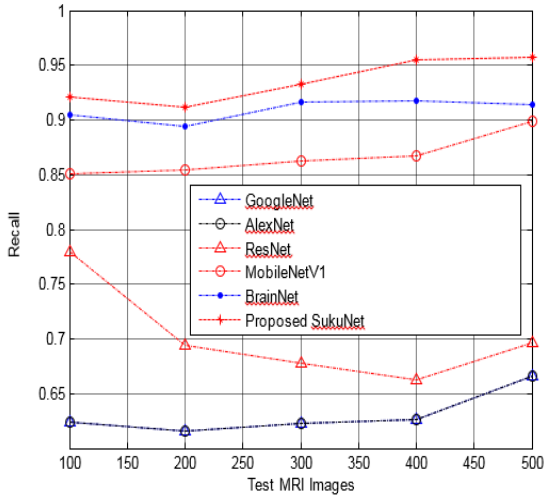

Figure 5: Recall

The recall results between the proposed SukuNet - MO model and existing deep neural network models like Google Net, AlexNet, ResNet, and MobileNetV1 are illustrated in Figure 5. The simulation results indicate that the proposed model outperforms the other deep learning models in terms of recall.

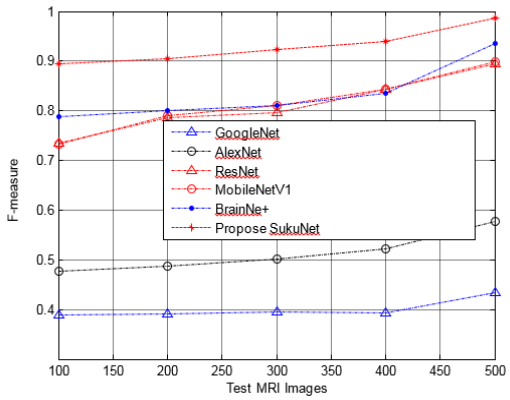

Figure 6: F1-Measure

The F1-Measure results, as demonstrated in Figure 6, compare the proposed SukuNetDenseNetFCM - MO model with existing deep neural network models such as GoogleNet, AlexNet, ResNet, and MobileNetV1. The simulation results indicate that the proposed model achieves a higher F1-score compared to the other deep learning models.

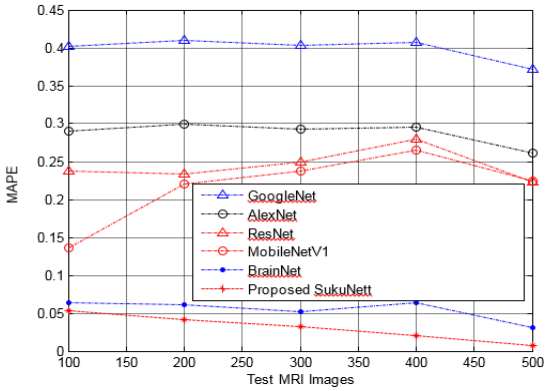

Figure 7: MAPE

Figure 7 shows the results of MAPE between the proposed SukuNet FCM MO with existing deep neural network models like GoogleNet, AlexNet, ResNet and MobileNetV1. The results of simulation show that the proposed model achieves reduced MAPE than the other deep learning models.

V. CONCLUSIONS

The research has presented a novel approach for MRI segmentation and classification that integrates morphological operations, DenseNet for ROI extraction, and SukuNet for classification. The results demonstrate significant improvements in

segmentation accuracy and classification performance compared to existing methods. By integrating regions outside of expanded areas such as the ventricles, the research can increase the selectivity of our model without compromising its sensitivity to the environment. It is possible that participants with suspected hydrocephalus could be eliminated from studies of Alzheimer disease and other neurodegenerative disorders with the use of an automated categorization system.

REFERENCES

[1] H. Arai et al., "Guidelines for management of idiopathic normal pressure hydrocephalus: Endorsed by the Japanese Society of Normal Pressure Hydrocephalus," Neurol. Med.-Chir., vol. 61, no. 2, pp. 63–97, 2021.

[2] S. D. Lolansen et al., "Inflammatory markers in cerebrospinal fluid from patients with hydrocephalus: A systematic literature review," Dis. Markers, vol. 2021, 2021.

[3] S. Gholampour and N. Fatouraee, "Boundary conditions investigation to improve computer simulation of cerebrospinal fluid dynamics in hydrocephalus patients," Commun. Biol., vol. 4, no. 1, pp. 1–15, 2021.

[4] Y. J. Bae et al., "Altered glymphatic system in idiopathic normal pressure hydrocephalus," Parkinsonism Relat. Disord., vol. 82, pp. 56–60, 2021.

[5] N. G. Pozzi et al., "Striatal dopamine deficit and motor impairment in idiopathic normal pressure hydrocephalus," Mov. Disord., vol. 36, no. 1, pp. 124–132, 2021.

[6] T. Hale et al., "multi-omic analysis elucidates the genetic basis of hydrocephalus," Cell Rep., vol. 35, no. 5, p. 109085, 2021.

[7] S. J. Schiff et al., "Brain growth after surgical treatment for infant postinfectious hydrocephalus in Sub-Saharan Africa: 2-year results of a randomized trial," J. Neurosurg. Pediatr., vol. 28, no. 3, pp. 326–334, 2021.

[8] J. M. Strahle et al., "Longitudinal CSF iron pathway proteins in posthemorrhagic hydrocephalus: Associations with ventricle size and neurodevelopmental outcomes," Ann. Neurol., vol. 90, no. 2, pp. 217–226, 2021.

[9] S. Gholampour and M. Bahmani, "Hydrodynamic comparison of shunt and endoscopic third ventriculostomy in adult hydrocephalus using in vitro models and fluid-structure interaction simulation," Comput. Methods Programs Biomed., vol. 204, p. 106049, 2021.

[10] R. Hu et al., "Long-term outcomes and risk factors related to hydrocephalus after intracerebral hemorrhage," Transl. Stroke Res., vol. 12, no. 1, pp. 31–38, 2021.

[11] T. Krejčí et al., "non-communicating hydrocephalus with a primary empty sella presenting with growth hormone deficiency and delayed puberty successfully treated by endoscopic third ventriculocisternostomy," Acta Neurochir., vol. 163, no. 2, pp. 511–514, 2021.

[12] T. Hale et al., "Machine learning predicts risk of cerebrospinal fluid shunt failure in children: A study from the Hydrocephalus Clinical Research Network," Childs Nerv. Syst., vol. 37, no. 5, pp. 1485–1494, 2021.

[13] Mládek et al., "Prediction of shunt responsiveness in suspected patients with normal pressure hydrocephalus using the lumbar infusion test: A machine learning approach," Neurosurgery, early access.

[14] Pahwa, O. Bali, S. Goyal, and S. Kedia, "Applications of machine learning in pediatric hydrocephalus: A systematic review," Neurol. India, vol. 69, no. 8, p. 568, 2021.

[15] O. M. Femi-Akinlosotu et al., "Deficits of learning and spatial memory are associated with increased pyknosis of pyramidal neurons of the hippocampus of adult rats with chronic hydrocephalus," West Afr. J. Med., vol. 38, no. 11, pp. 1042–1049, 2021.

[16] H. K. Talbot-Stetsko et al., "Ventricular volume change as a predictor of shunt-dependent hydrocephalus in aneurysmal subarachnoid hemorrhage," World Neurosurg., vol. 157, pp. e57–e65, 2022.

[17] K. Uyar et al., "multi-class brain normality and abnormality diagnosis using modified Faster R-CNN," Int. J. Med. Inform., vol. 155, p. 104576, 2021.